REVIEW

Check for updates

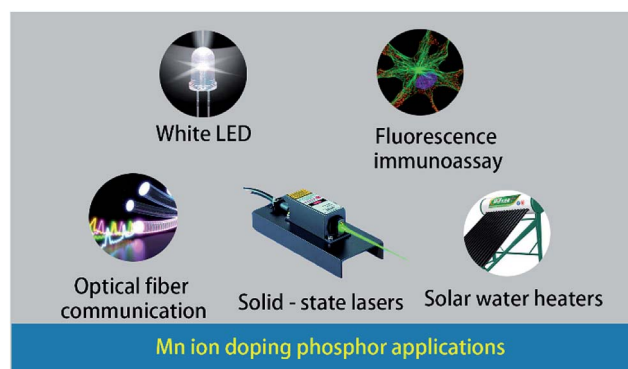# Research progress of Mn doped phosphors

Yamin Li, Shuai Qi, Panlai Li [ID] * and Zhijun Wang [ID] *

In this review article, Mn applications have been divided into three parts. We provide an overview of recent progress in developing Mn^{4+} doped red phosphors for promising application in warm white light-emitting diodes. In addition, we summarize reports on Mn^{2+} co-doped Eu^{2+} or Ce^{3+} phosphors that can produce white light with outstanding color rendering index (CRI) and color coordinates *via* energy transfer processes, and report the application of Mn^{2+} in green to NIR phosphors.

1 Introduction

The valence electron configuration of transition metal elements is $(n - 1)d^{1-8}ns^{1-2}$, with the common characteristic that the d orbitals are not full. Since the energy of the $(n - 1)d$ orbital is similar to that of the ns orbital, and the d electrons can completely or partially participate, there are no significant changes in the chemical properties from left to right in the same cycle. In addition, the transition metal elements can lose s electrons as well as d electrons; hence, the same element has a variety of valence states. Mn^{2+} and Mn^{4+} ions are commonly used as light-emitting centers. Nowadays, phosphor-converted white light emitting diodes (pc-WLEDs) based solid-state lighting has received much attention, due to the characteristics of high efficiency, high power efficiency, low applied voltage, reliability, long operation life and environmental friendliness, compared to other traditional lighting technologies, such as incandescent, halogen, xenon and fluorescent lamps.[1–5] In order to obtain highly efficient WLED devices, several aspects should be taken into account and optimized, including semiconducting components, phosphors and packaging technologies. Phosphors are indispensable components of pc-WLED devices, which can decide the color rendering index, correlated color temperature, rated average life and luminous flux. One method for obtaining these materials is to combine yellow-emitting phosphors with highly efficient (Ga,In)N blue LEDS. For blue chips, $Y_3Al_5O_{12}:Ce^{3+}$ (YAG:Ce) is the commonly used phosphor; however, due to the lack of the red component of YAG:Ce phosphor, this approach has a poor color rendering index and a high correlated color temperature, which cannot fulfill the requirements for general illumination.[6–9] According to Blasse, Mn^{4+} absorbs in the entire ultraviolet region and subsequently emits phosphorescence in the deep red (620–680 nm) region, due to transitions from $^2E \rightarrow {}^4A_2$,[10] which indicates that the phosphor doped Mn^{4+} can be a good candidate for red fluorescent powder. It has been observed that multi-phase

phosphor converted systems commonly lead to the strong reabsorption of the blue light by the red and green phosphors. Moreover, such a device is very complicated and expensive, and it is difficult to control the color balance. To solve the above-mentioned problems, single-emitting component phosphors with UV LEDs chips, which have excellent color rendering indexes and high luminous efficiencies, have been researched. One of the way to generate white light from single-composition phosphors is by co-doping the sensitizer and activator into a crystalline matrix, with the principle of energy transfer from sensitizer to activator, such as Eu^{2+}/Mn^{2+}, Ce^{3+}/Mn^{2+}. Various white light based single-composition phosphors have obtained, such as $CaAl_2Si_2O_8:Eu^{2+},Mn^{2+}$,[11] $Ba_3MgSi_2O_8:Eu^{2+},Mn^{2+}$,[12] $KMg_4(PO_4)_3:Eu^{2+},Mn^{2+}$,[13] $BaSi_3O_4N_2:Eu^{2+},Mn^{2+}$,[14] $Ca_2Gd_8(SiO_4)_6O_2:Ce^{3+}/Mn^{2+}$,[15] and $Ca_9La(GeO_4)_{0.75}(PO_4)_6:Ce^{3+},Mn^{2+}$.[16] Mn^{2+} is influenced by the crystal field, and hence it can easily change luminescence from green to deep red and even near-infrared (NIR). Because the near infrared light has the advantages of large penetration depth, less interference, *etc.*, it has become an important topic in the field of optical fiber communication, solid state lasers, light emitting markers and fluorescence immunoassays. The applications of Mn ion doped phosphors are shown in Fig. 1.

College of Physics Science & Technology, Hebei Key Lab of Optic-Electronic Information and Materials, Hebei University, Baoding 071002, China. E-mail: li_panlai@126.com; wangzj1998@126.com

Fig. 1 Applications of Mn ion doped phosphors.[11,17,50]

2 Application of Mn^{4+}

2.1 Introduction to red phosphors

To date, the most practical phosphor is the blue LED chip excited YAG:Ce^{3+}. In order to get white-light emission and a high CRI, improvements must be made by adding a high efficiency red emitting phosphor to the system to solve the problem of the lack of a red component; hence, several red phosphors have been developed. Red fluorescent powder can be divided into three categories: linear emission red phosphor excited by rare earth ions, broadband emission red phosphor excited by rare earth ions, and red phosphor excited by transition metals. With their own characteristics, excellent red phosphors can be obtained by a combination of these.

Linear-emission phosphors excited by the rare ions Eu^{3+} and Sm^{3+} have pure color and high luminous efficiency; however, there is no wide excitation spectrum in the blue and UV regions, which results in a lower luminous efficiency. It is feasible to broaden the excitation spectrum and improve the luminous efficiency, although the effect is not ideal, but this limits the practical application of linear phosphors. Therefore, the application of red emitting Sm^{3+} or Eu^{3+} ions doped phosphors is limited in the present W-LEDs, due to their sharp absorption peaks in the blue and UV region.

In order to create a warm WLED, the development of efficient red phosphors is necessary. The new phosphors are mainly based on rare earth-doped schemes, such as Eu^{2+}-doped nitrides, aluminates, oxynitrides and aluminosilicates. Among them, oxynitrides and nitrides have been the subject of maximal studies, due to their excellent performances, *e.g.*, chemical stability and high thermostability; however, these materials must be synthesized at high temperatures and pressures. The strict preparation conditions and high price of raw materials lead to this phosphor being quite expensive. In addition, the reabsorption of the coexistent green emission of WLEDS is not avoided for Eu^{2+}-doped red phosphors with blue absorption.[18]

2.2 Luminescence properties of transition metal ions

Transition metal ions have unfilled d orbitals, with the electronic configuration of $3d^n$ $(0 < n < 10)$. The Hamilton operator is as follows:

$$H = H_0 + H_{CF} + H_C + H_{SO} \tag{1}$$

where H_0 includes the kinetic energy of electrons and the Coulomb energy of the nucleus acting on the electron. H_C is the Coulomb energy between electrons, H_{SO} is the spin–orbit coupling energy and H_{CF} is the energy of the crystal field.

The 3d electron is in the outer layer, which is sensitive to the crystal environment; hence the H_{CF} and the Coulomb energy between electrons (H_C) can be compared. The crystal-field spectral term usually has two types of energy representations with weak crystal field and strong crystal field. We always apply the strong crystal field to deal with problems. The first consideration is how the d orbital is affected by the tetrahedral and octahedral crystal fields. The crystal field causes the five degenerate d orbitals to split into the doubly degenerate e_g and triply degenerate t_{2g}. The distance between e_g and t_{2g} is denoted as 10Dq, and Dq is a parameter to characterize the field strength of the octahedral.

With the single electron orbital wave function of e_g and t_{2g} as basic functions, considering the impact of Hc, a new intrinsic function is characterized by $^{2S+1}\Gamma$, where S is the total spin, and there is an irreducible representation of the octahedral group of the intrinsic state. The $^{2S+1}\Gamma$ spectral term is similar to that used in the study of the free ion ^{2S+1}L spectra of rare earth elements. The spin orbit interaction H_S in transition metal ions is weaker than that of rare earth ions, which is usually treated by the perturbation theory and the deviation of the crystal field in the octahedral symmetry. These interactions cause $^{2S+1}\Gamma$ to split into multiple states. The complete theoretical treatment of the transition metal ions eigenstate was given by S. Sugano and Y. Tanabe.[19] Direct coulombic interactions $(H_C)_{dir}$ between electrons are characterized by Racah parameters A, B, C

$$(H_C)_{dir} = \sum_k f_k F^{(k)} \tag{2}$$

where the fitting parameter

$$F^{(k)} = e^2 \int_0^\infty \int_0^\infty \frac{r_<^k}{r_>^{k+1}} \left[R_i(r_i) R_j(r_j) \right]^2 dr_i dr_j \tag{3}$$

For the ll′ configuration, the k in $F(k)$ is an even number from 2 to min (2l, 2l′). For transition metal ions with 3d electrons, the values can be 0, 2, 4. The relationship between Racah parameters and $F(k)$ is as follows:

$$B = \frac{1}{49}F^{(2)} - \frac{5}{441}F^{(4)} \tag{4}$$

$$C = \frac{35}{441}F^{(4)} \tag{5}$$

$$A = F^{(0)} - \frac{1}{9}F^{(4)} \tag{6}$$

Since the A parameter only affects the energy levels, we only consider B and C. The ratio of B/C for the all the transition metal ions is almost equal to 4.5, which can be seen as approximately constant. The distance between different spectra of each ion depends on the two parameters, Dq and B. In the work of S. Sugano and Y. Tanabe, the Tanabe–Sugano (T–S) (Fig. 2)[19] diagram shows the relationship between the energy levels of metal ions E/B and crystal field strength Dq/B of the d^2–d^8 configurations in the crystal field. From the T–S graph, we can identify each excitation peak corresponding to energy levels in the excitation spectra.

2.3 The transition of Mn^{4+} in the host[20]

Mn^{4+} doped materials, such as oxides and fluorides, are commonly used as red emitting phosphors. It was discovered that the Mn^{4+} ion can only be stabilized in an octahedral lattice site where it commonly shows strong and broad adsorptions

Fig. 2 Tanabe–Sugano diagram for the d^5 electron configuration.[19]

Fig. 3 Tanabe–Sugano diagram for the d^3 electron configuration in an octahedral crystal field.[21]

ranging from 300 to 480 nm and emits red light between 600 and 700 nm with 5 sharp peaks. As the lowest energy state $^2E(t_2^3)$ hardly changes in different crystal fields, the luminescence properties are very similar from host to host, but intensely depend on the covalence of the Mn^{4+}-ligand bonding.[18] Moreover, Mn is magnetic and will produce local magnetic ions when introduced into luminescent materials; therefore, Mn may have huge potential application value.

Doped in a solid, the Mn^{4+} ion has a strong crystal field, due to its highly effective positive charge. Consequently, the spin-forbidden $^2E_g \rightarrow {}^4A_{2g}$ transition (sharp line) always controls the emission spectrum of Mn^{4+}, while two broad bands corresponding to the $^4A_{2g} \rightarrow {}^4T_{1g}(^4F)$ and $^4A_{2g} \rightarrow {}^4T_{2g}$ spin-allowed transitions are observed in the excitation spectra. The third spin-allowed transition ($^4A_{2g} \rightarrow {}^4T_{1g}(^4P)$) frequently remains under cover by the host lattice absorption and the charge transfer. The $^2E_g \rightarrow {}^4A_{2g}$ transition has a wide variation, which is due to the energy of the ^2E_g state in the d^3 electronic configuration being independent of crystal field (Fig. 3).[21]

2.4 Spectroscopic parameters of Mn^{4+} in different hosts[21]

The positions of zero-phonon lines in the $^2E_g \rightarrow {}^4A_{2g}$ spin-forbidden transition of the Mn^{4+} ion, 'host cation ligand' bond distance and Racah parameter B have been summarized numerous crystals. On an average, the distance from Mn^{4+} to ligand in the fluoride crystals (about 1.67–1.86 Å) is the shortest

and the following trends (Fig. 4) are formulated from the graphical representations of the data gathered in Table 1, which is suitable for most compounds. The B values are greater in fluorides and thus, the emission lines of ^2E_g–$^4A_{2g}$ are significantly increased in oxides and in materials with the garnet structure (up to 2.11 Å), as shown in Table 1. The energy difference among the $^4A_2 \rightarrow {}^4T_2$ and the $^4A_2 \rightarrow {}^4T_1$ transitions and the Racah parameter B can be derived from the expression[22–24]

$$\frac{Dq}{B} = \frac{15(x-8)}{x^2 - 10x} \qquad (7)$$

where x is defined as

$$x = \frac{E\left(^4A_{2g} \rightarrow {}^4T_{1g}\right) - E\left(^4A_{2g} \rightarrow {}^4T_{2g}\right)}{Dq} \qquad (8)$$

The Racah parameter C can be evaluated by the following expression, according to the peak energy of $^2E_g \rightarrow {}^4A_{2g}$ obtained from the emission spectrum.

$$\frac{E\left(^2E_g - {}^4A_{1g}\right)}{B} = 3.05\frac{C}{B} + 7.9 - 1.8\frac{B}{Dq} \qquad (9)$$

The local crystal-field strength Dq is determined by the mean peak energy of the $^2A_2 \rightarrow {}^4T_2$ transition according to the following expression:
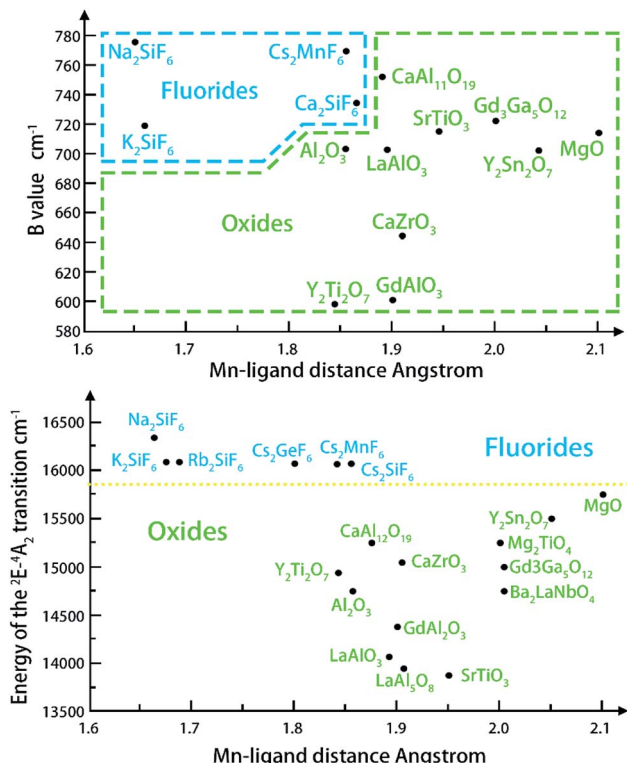
Fig. 4 Relationship between the Mn^{4+} ligand[21] bond distance and the Racah parameter B (top), and the position of the ^2E_g level (bottom).[21]

$$Dq = \frac{E\left(^4T_{2g} - ^4A_{2g}\right)}{10} \quad (10)$$

The ^2E_g level is always lower for oxides; however, the value of B is also close to that of fluorides in some special cases (Fig. 4). What causes the condition is that the position of the ^2E_g level also depends on the value of the second Racah parameter C.[25-27]

Such a distinct and explicit separation of fluorides and oxides with respect to the energy position of the ^2E_g level indicates the potential role of the Mn^{4+} ion as a reliable indicator of covalency/ionicity of a particular host. On the other hand, Mn^{4+} luminescence exhibits sharp emission lines and broad excitation bands in the ultraviolet–blue region, which makes it suitable for excitation by UV and decreases the re-absorption effect when mixing with other yellow and green phosphors. With so many unique features, Mn^{4+} can meet the requirement of an ideal red phosphor for warm LEDS. Moreover, the easy to obtain and cheap manganese raw materials are able to reduce the red phosphors. As a consequence, many researchers have focused on developing the Mn^{4+} activated red phosphors (Table 2).

2.5 Examples of Mn^{4+} doped red phosphors

Numerous researchers have focused on the oxide host, due to their outstanding performance such as high stability. Peng *et al.* have synthesized an efficient red oxide phosphor $Sr_4Al_{14}O_{25}:Mn^{4+}$,[28] which is prepared by a traditional solid-state reaction in much milder conditions. The red emission intensity

Table 1 Summary of some spectroscopic and structural characteristics

Host	Cation–ligand distance, Å	Racah parameter B, cm^{-1}	Position of the ^2E_g level, cm^{-1}
Na$_2$SiF$_6$	1.674	775	16 207
K$_2$SiF$_6$	1.6829	719	16 109
Rb$_2$SiF$_6$	1.689	625	16 082
Cs$_2$GeF$_6$	1.798		16 038
Cs$_2$SiF$_6$	1.867	722	16 033
Cs$_2$MnF$_6$	1.857	775	16 031
Mg$_2$TiO$_4$	1.948	700	15 253
CaZrO$_3$	1.9137	650	15 054
Gd$_3$Ga$_5$O$_{12}$	2.005	722	14 980
Al$_2$O$_3$	1.858	700	14 786
GdAlO$_3$	1.903	600	14 347
LaAlO$_3$	1.895	700	14 045
LiAl$_5$O$_8$	1.900		13 966
SrTiO$_3$	1.952	719	13 827
Y$_2$Ti$_2$O$_7$	1.844	600	14 956
Y$_2$Sn$_2$O$_7$	2.048	700	15 563
GaAl$_{12}$O$_{19}$	1.8791	750	15 241
MgO	2.1135	722	15 809
Ba$_2$LaNbO$_6$	1.9975	670	14 680

Table 2 Known compounds of red phosphors doped with Mn^{4+}

Chemical composition	λ_{ex} (nm)	λ_{em} (nm)	Incorporated site	Ref.
BaTiF$_6$:Mn^{4+}	367, 468	634	Ti^{4+}	35
Na$_2$SiF$_6$:Mn^{4+}	360, 460	600–650	Si^{4+}	36
Na$_3$GaF$_6$:Mn^{4+}	460	630	Ga^{3+}	37
Sr$_2$MgAl$_{22}$O$_{36}$:Mn^{4+}	312	658	Al^{3+}	38
CaAl$_{12}$O$_{19}$:Mn^{4+}	325, 457	600–700	Al^{3+}	39
Li$_2$MgGeO$_4$:Mn^{4+}	323	671	Ge^{4+}	40
(K,Rb)$_2$Ge$_4$O$_9$:Mn^{4+}	295, 460	620–727	Ge^{4+}	41

of $Sr_4Al_{14}O_{25}:Mn^{4+}$ is greater than that of the reported commercial phosphors, such as $(K,Rb)_2Ge_4O_9:Mn^{4+}$ (ref. 29) and $CaAl_{12}O_{19}:Mn^{4+}$.[30]

A series of novel red emitting $Mg_3Ga_2GeO_8$ under near-UV excitation was successfully synthesized by Ding *et al.* with the traditional high-temperature solid-state reaction.[31] In this $Mg_3Ga_2GeO_8$ system, there is one tetrahedral site, which is occupied by Ge^{4+}/Ga^{3+}, and an octahedral site, occupied by Mg^{2+}/Ga^{3+}. According to radius analysis and luminescence properties of $Mg_3Ga_2GeO_8:x\%Mn^{4+}$, we can conclude that Mn^{4+} reliably occupies the Mg^{2+}/Ga^{3+} site in this system. When using $MnCO_3$ as the raw material, the intensity of the emission is relatively weak, compared to the sample of MnO_2 as the raw material and the peak shape does not change. In the $MnCO_3$, the same Mn^{2+} can just be oxidized to Mn^{3+}, rather than Mn^{4+}, as shown in Fig. 5. The emission properties of $Mg_3Ga_2GeO_8:x\%Mn^{4+}$ are also shown in Fig. 5. It can be easily seen that the emission intensities reach a maximum at $x = 0.5\%$ and the calculated full-width at half-maximum (FWHM) of the Mn^{4+} emission spectrum is 24 nm, which indicates that the $Mg_3Ga_2GeO_8:x\%Mn^{4+}$ phosphor

possesses high color purity. Furthermore, $Mg_3Ga_2GeO_8$:0.5% Mn^{4+} exhibits outstanding quantum efficiency (64.7%).

The oxide matrix with strong covalent, low thermal vibration and weak polarizability is favourable for red light emission. The Mn^{4+} doped $Y_3Al_5O_{12}$ phosphor was prepared by a high temperature solid state reaction method. Huang et al. synthesized the $Y_3Al_5O_{12}$:Mn^{4+} red phosphor and explored its luminescence properties. At 467 nm, this phosphor emits red light.[31] The main emission peaks are at 643 and 670 nm, all from the $^5E \rightarrow {}^4A_2$ transition of Mn^{4+} in $Y_3Al_5O_{12}$:0.01Mn^{4+}. The CIE of the $Y_3Al_5O_{12}$:0.01Mn^{4+} phosphor is (0.701, 0.299) located in the red area. The excitation spectrum of the emission peak at 670 nm is composed of 400, 450, 468, 474, 482 and 494 nm wide excitation bands.

Novel red-emitting phosphors $K_2BaGe_8O_{18}$:Mn^{4+} were synthesized via the high temperature solid-state reaction method.[32] The excitation spectrum of $K_2BaGe_8O_{18}$:Mn^{4+} monitored at 666 nm shows a wide band with two evident peaks at 319 and 468 nm. Upon 468 nm excitation, the emission spectrum presents a narrow band from 600 to 700 nm (red region) with the maximum emission at around 666 nm, which originates from the ^2E_g–$^4A_2$ transition of Mn^{4+} in the GeO_6 octahedral environment, as shown in Fig. 6; the CIE coordinates of the phosphors are (0.702, 0.298) and the QY is 32.9% upon 365 nm excitation. The results indicate that this kind of phosphor can be a supplement of red-components in UV and blue light excited w-LEDs.

In the oxide matrix, Mn^{4+} ions replace cations such as Al^{3+}, Si^{4+}, Zr^{4+}, Ti^{4+}, Ge^{4+}, and occupy the center of the octahedron. When Mn^{4+} replaces ions with different valences, charge compensation is required. Therefore, the emission intensity of the phosphor can be enhanced by performing charge compensation. Mg^{2+} has been very extensively researched as a highly efficient charge compensator. The substitution of the Mg^{4+}–Mg^{2+} ion pair to replace the Al^{3+}–Al^{3+} ion pair was made under the condition that no additional charge compensation and oxygen atoms are required. Ge^{4+}, Ca^{2+}, Li^+, Na^+, K^+, Cl^- can also be used as charge compensators to enhance the luminescence properties of red phosphors.[33,34] Different charge compensators have different effects on the red luminescence properties of Mn^{4+}.

The chemical stability of fluorides is appropriate, and the phonon energy is relatively low, so fluorides can be used as the host material for various luminescent rare earth ions. Na_2SiF_6:Mn^{4+} red fluoride phosphors have been synthesized by the exothermic reduction reaction method, as shown in Fig. 7.[36] The phosphors have intense blue-light absorption and strong narrow-band red emission. When the Na_2SiF_6:Mn^{4+} red phosphor was fabricated, a prominent improvement in the CRI of white LEDs was observed. The Na_2SiF_6:Mn^{4+} phosphors have efficient red luminescence excited by blue light, which is a potential candidate for improving the color reproducibility of white LEDs with simple post-processing, a short reaction time and high yield.

Mn^{4+}-activated fluoride phosphors, such as A_2BF_6 (A = Na, K, Rb, Cs; A_2 = Ba, Zn; B = Si, Ge, Ti, Zr, Sn), have attracted

Fig. 6 (1) PL spectra of $K_2BaGe_8O_{18}$:Mn^{4+} with different concentrations, and PL excitation spectra of the $K_2BaGe_8O_{18}$:0.002Mn^{4+} sample monitored at 666 nm and 654 nm. (2) Chromatic CIE coordinates, quantum yields and variation of emission intensity depending on the temperature of the representative $K_2BaGe_8O_{18}$:Mn^{4+}.[32]

Fig. 5 (1) PL properties of samples with different Mn sources and doped sites. (2) PL under 419 nm excitation of the $Mg_3Ga_2GeO_8$:x% Mn^{4+} series phosphors.[31]

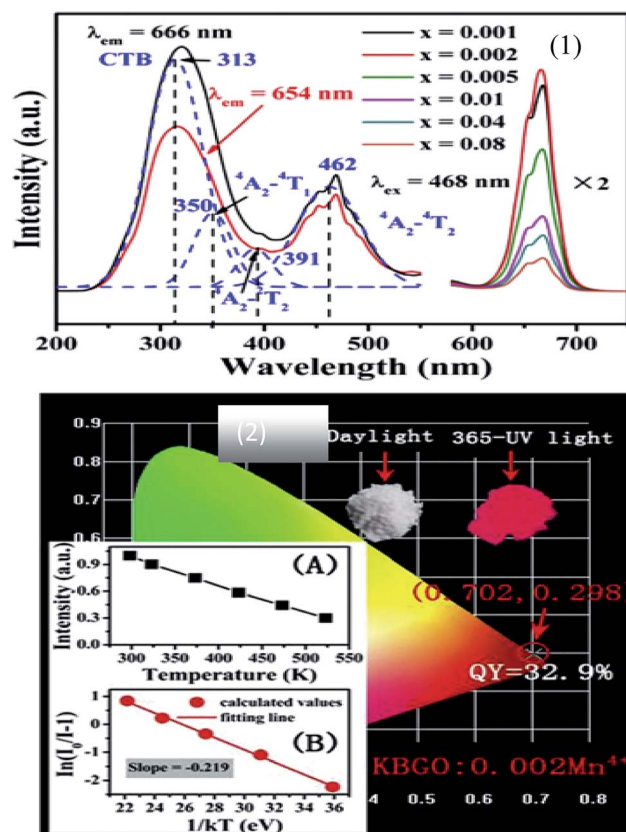Fig. 7   (1) Excitation and emission spectra of the Na$_2$SiF$_6$:Mn^{4+} phosphor with HF concentrations of (a) 10, (b) 20, (c) 30, and (d) 40 wt%. (2) Luminescence spectra based on the Na$_2$SiF$_6$:Mn^{4+} phosphor under various drive currents.[36]

Fig. 8   (a) Concentration dependent emission spectra of K$_3$AlF$_6$:Mn^{4+}. (b) Electroluminescence spectra of prototype LEDs, employing K$_3$AlF$_6$:Mn^{4+} as the red converter component, commercial yellow YAG:Ce^{3+} and a blue InGaN chip at a 40 mA drive current.[42]

considerable attention as highly promising red phosphors for warm white light emitting diodes (w-LEDs). These fluoride phosphors have been synthesized via traditional chemical routes with HF-solution. In addition to the possible dangers of hypertoxic HF, the uncontrolled precipitation of fluorides and the extensive processing steps produce large morphological variations, limiting its application. Recently, Song made a prototype w-LED with K$_3$AlF$_6$:Mn^{4+} as the red light component, via an efficient and water-processable cation-exchange green route.[42] Combined with YAG:Ce^{3+}, the prototype of the sample shows an efficient luminous efficacy beyond 190 lm W^{-1}, along with an excellent color rendering index (CRI, R_a = 84) and a lower correlated color temperature (CCT = 3665 K), as shown in Fig. 8.

Thus far, Mn^{4+} as an activator doped oxide/fluoride red phosphor has attracted significant attention, due to its special advantages such as relatively simple synthesis methods and low cost. The spectral positions produced by the $^2E_g \rightarrow {}^4A_{2g}$ transition can be modified, and the excitation region of the phosphor is located in the ultraviolet and blue band. Therefore, the Mn^{4+} doped red phosphor can be used as a substitute for rare earth doped red phosphors, and has a bright future in the field of warm white LEDs.

Although a large number of Mn^{4+} doped red phosphors have been fully studied, there are still some questions worthy of further exploration. For the Mn^{4+} doped oxide host phosphor, it is desirable to achieve a blue shift of emission from deep red to orange/red and enhanced absorption in the blue wavelength region. One possible solution is doping to increase the absorption in the blue wavelength region for

Sr$_4$Al$_{14}$O$_{25}$:Mn^{4+} doped Mg^{2+}; because the neighboring Mn^{4+}–Mn^{4+} is replaced by Mn^{4+}–Mg^{2+}, the non-radiative decay rate of the ^2E_g state decreases and the luminous intensity of the phosphor is enhanced. For fluoride phosphors, how to improve their thermal stability and resistance to humidity needs further study. Surface treatment by external coating can improve the thermal stability and moisture resistance. Finally, the quantum efficiency of materials can be further improved by optimizing synthesis methods and reducing the lattice defects of materials.

3   Application of Mn^{2+}

3.1   Application of Mn^{2+} in green to NIR phosphors

Most phosphors applied in white LEDs are oxides, sulfides or nitrides doped with rare-earth ions, which play a significant role in controlling the color of the light. Most of these rare-earth ions are very expensive and some chloride and oxide doped rare-earth elements are toxic and harmful, which limit their

development. Consequently, the search for a cheap and nontoxic phosphor has become an important research area and Mn^{2+} doped oxides and nitrides have become hot research topics. With the d electrons within the 3d shell, Mn^{2+} emission can be affected by the crystal field, which results in the emission changing from green to red. When Mn^{2+} is located in the tetrahedral crystal field, it can emit green light. In other words, through changing the crystal field conditions, the spin-forbidden Mn^{2+} forbidden d–d transition ($^4T_1 \rightarrow {}^6A_1$) can emit green light.

Rare earth ions (Eu^{2+}, Eu^{3+}, or Pr^{3+}) or transition metal elements (Cr^{3+} or Mn^{2+}) can serve as luminescence centers in NIR phosphors. However, for biological applications, these hygroscopic sulphides of Eu^{2+} show a succession of problems in metal-activated oxide compounds, such as Cr^{3+} or Mn^{2+}-doped phosphors, which have outstanding chemical stability and suitable chemical instability. Lately the focus has shifted to the transition-emission range in the optical window (from 650 to 1300 nm) and long-lasting persistent luminescence. With the advantages of high signal to noise ratio, deep tissue penetration, and maximum transparency for silicon-based optical fibers and so on, near infrared (NIR) emitting materials have distinct potential for medical diagnostics, laser systems, and optoelectronic devices.[43–45] On the basis of coordination and the T–S diagram, due to weaker crystal symmetry (angular constraints) and stronger ligand field strength (interionic distance) than that of the four/six-coordinated environments, it is feasible to speculate that the five/seven-coordinated environments of the Mn^{2+} ion are good for NIR emission generation.[46–49] There is a complete list of known green to NIR persistent phosphors activated by Mn^{2+} in Table 3.

The rare-earth-free narrow-band green-emitting $KAlSi_2O_6$:Mn^{2+} phosphor has been synthesized by Ding et al. The excitation and emission spectra are shown in Fig. 9. The five distinct peaks of PL excitation are in good agreement with the Mn^{2+} absorption transitions; specifically, it can match blue GaN chips, which make its application in white LEDs possible. Moreover, a green light emission peak at 513 nm with full-width at half-maximum of 30 nm can be seen from Fig. 9, which is attributed to the spin forbidden d–d transition ($^4T_1 \rightarrow {}^6A_1$) of Mn^{2+}. The electrons could be relaxed from these excited states to the $^4T_1(G)$ state by a non-radiative relaxation process and then be transferred back to the ground state $^6A_1(S)$, emitting the characteristic green (513 nm) light. The CIE color coordinates of the $KAlSi_2O_6$:Mn^{2+} phosphor were calculated to be $x = 0.27$ and $y = 0.64$, which are much closer to the standard green coordinates (0.21, 0.71). The integrated emission intensity of KAS:3% Mn^{2+} decreased to 67.6% (250 °C) of the initial value (25 °C). The chromaticity coordinates of the fabricated white LED are (0.35, 0.36) with CCT of 4775 K. It is demonstrated that the $KAlSi_2O_6$:Mn^{2+} phosphor could be simulated to blue-LED for producing efficient white-light.

Moreover, good performance Mn^{2+} doped Na_2MgGeO_4 phosphors have been reported. Under UV or electron beams, the samples show bright green emission, which is ascribed to the $^4T_1(4G)$–$^6A_1(6S)$ transition of the Mn^{2+} ions. Based on this transition, the following phosphors were developed:

Table 3 Known compounds of green to NIR persistent phosphors activated by Mn^{2+}

Host material	Incorporated site	Emission region (nm)	Ref.
$CdSiO_3$	Cd^{2+}(VI)	550–720	50
$MgGeO_3$	Mg^{2+}(VI)	600–720	51
$Li_2ZnGe_3O_8$	Zn^{2+}(VI)	700–900	52
$Ga_3(PO_4)_2$	Ca^{2+}(VI)	600–750	53
$Ga_9Ln(PO_4)_7$	Ca^{2+}(VI)	600–750	54
$(Mg_{1-x}Zn_x)_{2.97}(PO_4)_2$	Mg^{2+}/Zn^{2+}(VI)	630–800	55
$KMgBO_3$	Mg(VI)	600–700	56
$MgAl_2O_4$	Mg(IV)	500–560	57
Na_2MgGeO_4	Mg(IV)	500–550	58
$KAlSi_2O_6$	Al/Si(IV)	500–540	59
Zn_2GeO	Zn(II)	500–570	60

$Na_2Mg_{1-x}SiO_4$:xMn^{2+} green phosphors, with CIE coordinates of (0.163, 0.631) and CTT value of 8643 K,[61] $NaAl_{11}O_{17}$:Mn^{2+} green phosphors, with CIE chromaticity coordinates of (0.0725, 0.6468), and quantum efficiency of 67.84%, with excitation of 424 nm,[62] Zn_2SiO_4:Mn^{2+} green phosphors, which exhibit widely tunable CCTs ranging from 3200 to 7000 K and color rendering indices up to 85%, depending on the mixture ratio.[63] Those phosphors with good performance indicators can be candidates for high power pcWLED applications. In addition, $MgAl_2O_4$:Mn^{2+},[57] Zn_2SiO_4:Mn^{2+},[64,65] green phosphors have also been reported.

Song et al. have reported the realization of single-band NIR UC emission in a Mn^{2+}-doped $KZnF_3$ nanostructure by a heavy doping strategy.[66] Fig. 10 shows the emission spectra of $KZn_{1-x}Mn_xF_3$ upon 396 nm light excitation. There is a single visible emission located at 585 nm when Mn^{2+} concentration is less than $x = 0.10$, corresponding to the $^4T_{1g}(G) \rightarrow {}^6A_{1g}(S)$. An anomalous NIR emission band located at 770 nm appears when $x = 0.10$, while at $x = 0.30$, there is a sharp decrease due to the concentration quenching effect, where visible and NIR emission bands are featured from two different emission centers. The luminescence decay curves (Fig. 10(c) and (d)) were studied in order to obtain more insight into the active centers. The visible emission exhibited single exponential decay at a low concentration ($x = 0.01$ and 0.05), and the decay lifetime was estimated by the following equation:

$$I(t) = I_0 + A \exp(-t/\tau) \tag{11}$$

where $I(t)$ and I_0 represent the emission intensity at time t and 0, respectively, A is a constant, and τ is the decay lifetime. For Mn^{2+}-heavy doping ($x = 0.10$–0.30), the visible emission exhibited non-exponential decay behavior, probably associated with the prevailing non-radiative transition, which is expressed by the mean decay lifetime (τ_m) estimated by

$$\tau_m = \int_{t_0}^{\infty} I(t)/I_{max} \, dt \tag{12}$$

where $I(t)$ is the luminescence intensity at t and $I_{max} = I(0)$. The non-radiative loss occurring among the Mn^{2+} ions as the Mn^{2+} concentration increases can be demonstrated from the monotonously shortened decay lifetime of the two emission bands.

Fig. 9 (a) Photoluminescence excitation of $KAlSi_2O_6$:Mn^{2+}; (b) photoluminescence emission spectra of $KAlSi_2O_6$ phosphors, inset: dependence of the emission intensity of $KAlSi_2O_6$:Mn^{2+} phosphors on Mn^{2+} content; (c) the excitation and emission transitions of Mn^{2+} ions; (d) the CIE chromaticity coordinates and their respective quantum yields. The inset shows the phosphor simulated white light using blue (455 nm) LED.[59]

To study the reason for the observed unusual NIR emission in $KZn_{1-x}Mn_xF_3$, the crystal structure of $KZnF_3$ and the activation process of Mn^{2+} were further analyzed. $KZnF_3$ has a typical cubic perovskite structure with a $Pm\bar{3}m$ space group with its lattice constant $a = 0.405$ nm, as shown in Fig. 10(a). Zn^{2+} is substituted by the incorporated Mn^{2+} ions, leading to the formation of $Mn^{2+}(Zn^{2+})$–$Mn^{2+}(Zn^{2+})$ dimmers, especially at a high doping concentration. The ground state ($^6A_1$, $S = 5/2$) and the first excited state ($^4T_1$, $S = 3/2$) are split due to the exchange interaction between Mn^{2+} and Mn^{2+} ions, which are mainly governed by the linear combination of two spin states, S_i and S_j (i.e., $(S_i + S_j)$, ..., $(S_i - S_j)$).[67] Therefore, the spin state is $S = 5, 4, 3, 2, 1$, and 0 for the ground state ($^6A_{1g}(S)^6A_{1g}(S)$) and $S = 4, 3, 2$, and 1 for the first excited state ($^6A_{1g}(S)^4T_{1g}(G)$). The Mn^{2+}–Mn^{2+} dimmers can also serve as the chromophoric centers, and the observed NIR luminescence is most likely related to the radiative transition from the excited state ($S = 1$) to the ground state with various spin components. There could be a shift in the emission peak caused by the changes in the spin components. The reason for decay lifetime shortening may be that the spin selection rule has changed from spin forbidden ($S = 5/2 \rightarrow S = 3/2$) to spin allowed ($S = 1 \rightarrow S = 1$), hence, it is reasonable to suggest that the NIR emission in $KZn_{1-x}Mn_xF_3$ originates from the $^6A_{1g}(S)^4T_{1g}(G) \rightarrow ^6A_{1g}(S)^6A_{1g}(S)$ transitions of coupled Mn^{2+}–Mn^{2+} dimmers.

Near-infrared (NIR) emitting $Li_2ZnGe_3O_8$ (LZG):xMn^{2+} has been synthesized by a conventional solid state reaction.[52] The excitation spectrum (PLE) and emission spectrum (PL) of the LZG:xMn^{2+} ($x = 0.005, 0.01, 0.03, 0.05, 0.07, 0.10, 0.15, 0.20$) phosphors are presented in Fig. 11(a) and (b), respectively. The emission spectrum shows a broad emission band from 650 to 900 nm, with the main peak at 832 nm. The luminescence properties can be strongly affected by the crystal field within the 3d shell with an increase in Mn^{2+} concentration. The PL ($\lambda_{em} = 832$ nm) intensity rapidly increases, while above this maximum intensity (0.03), a concentration quenching phenomenon occurs, as shown in Fig. 11(d). Essentially, quenching impurities cause concentration quenching, a decline in the emission intensity, as shown in Fig. 11. Non-radiative energy transfer, which include exchange interactions, radiation

Fig. 10 (a) TEM image of KZn$_{0.80}$Mn$_{0.20}$F$_3$ nanocrystals and a typical nanocrystal (inset). (b) Emission spectra and (c) luminescence decay curves at 585 nm and (d) 770 nm for KZn$_{1-x}$Mn$_x$F$_3$ ($x = 0.01–0.40$). The inset in (b) shows the emission spectrum of KMnF$_3$. The emission spectra and luminescence decay curves were obtained upon excitation with 396 nm light.[66]

reabsorption and multipolar interactions between Mn^{2+} ions within a certain distance, lead to concentration quenching. According to calculations, the concentration quenching of Mn^{2+} ions originates from quadrupole–quadrupole interactions. Besides, the phosphor has a good thermal stability, which expands the scope of its application.

Energy transfer between ions is a rather common and very important physical phenomenon, mainly through physical processes such as collision, energy exchange, and re-absorption of radiation and radiationless transition processes, which cause the ion energy transfer to other ions. Due to the relatively rich energy levels of transition metal ions, especially in the crystals, the energy splitting is affected by the influence of the crystal field, thus becoming more intensive. At this point, there may be the possibility of energy differences between the two levels of the transition metal ions, equal to the difference between other ions. In order to achieve the energy transfer between ions, radiative or radiationless transition processes occur very easily under the action of multipole moments.

Radiationless transitions play a significant role in photophysics, photobiology and photochemistry, and include

internal conversion (IC) (spin-allowed process) and intersystem crossing (ISC) (spin-forbidden process). A simplified Jablonski diagram is presented in Fig. 12, which describes the elementary processes of molecular luminescence.[68]

Absorption

$$S_0 + \hbar w \xrightarrow{k_a} S_1 \tag{13}$$

Fluorescence

$$S_1 \xrightarrow{k_r} S_0 + \hbar w' \tag{14}$$

Internal conversion

$$S_1 \xrightarrow{k_{ie}} S_0 \tag{15}$$

Intersystem crossing

$$S_1 \xrightarrow{k_{ise}} T_1 \tag{16}$$
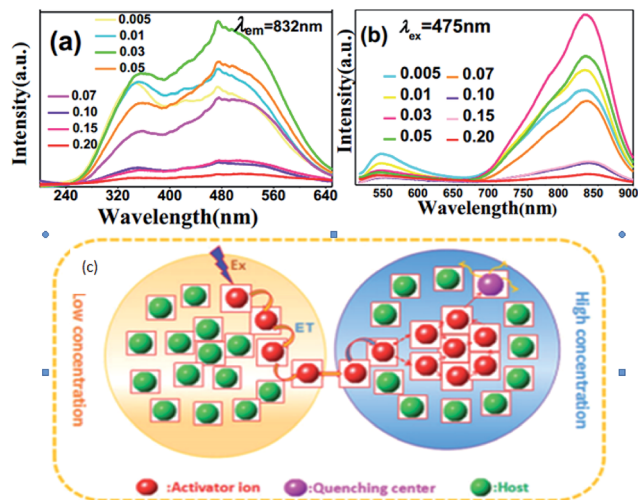
Fig. 11 (a) PLE and (b) PL spectra of the LZG:xMn^{2+} samples ($0 < x <$ 0.2). (c) A diagram of the concentration quenching process.[52]

Fig. 12 Elementary photophysical processes of molecular luminescence.[68]

Phosphorescence

$$T_1 \xrightarrow{k'_r} S_0 + \hbar w'' \qquad (17)$$

Intersystem crossing

$$T_1 \xrightarrow{k'_{ise}} S_0 \qquad (18)$$

These elementary processes determine whether a molecule can be a good candidate for a dye molecule for organic solar cells or LED. Besides, there are two other significant elementary processes described in the following:

Phonon-induced electron transfer

$$DA \xrightarrow{hv} D^*A \rightarrow D^+A^- \qquad (19)$$

Phonon-induced energy transfer

$$DA \xrightarrow{hv} D^*A \rightarrow DA^* \qquad (20)$$

All the processes involve two electronic states, *i.e.*, they are non-adiabatic in nature. Vibrational relaxation (VR) exists in molecular luminescence as a non-radiative process, which can happen in either the ground or excited electronic states. The radiative transfer process is also called resonant transmission, if there is a near field force interaction between the two centers and if the energy of light radiation transfer can be one atom to 10 nm, without the help of other nearest neighbor atoms. Dexter first introduced the transfer mechanism to the energy transfer process between the centers of the luminous material, and derived a formula for the probability of resonance energy transfer between the centers. There is an assumption that emission from the ion overlaps another ion, absorbing light, so the light emitting radiation energy is absorbed by another ion, and energy transfer occurs. The former is called the energy sensitizer and the

latter is called the activator. Overlap between the emission spectra of the sensitizer and the excitation spectra of the activator is a prerequisite for the occurrence of resonant transmission. Resonant transmission is a quite significant means of energy transfer in the material activated by rare earth or transition metal elements and organic crystals. In this way, there are two centers S and A, where the center initial state is S* + A, *i.e.*, the S center is in the excited state, the A center is in the ground state. The final state is S + A, *i.e.*, the S center is back to the ground state, and the A center is in the excited state. Taking S and A as the dipoles, the transition probability from the initial state to the final state is the S, A resonance energy transfer probability P_{SA}:

$$P_{SA} = \left(\frac{R_0}{R}\right)^6 \times \frac{1}{\tau_S^*} \qquad (21)$$

where R is the distance between the center of S and A and τ_S^* is the measured lifetime of S* state, and the R_0 is defined as:

$$R_0^{\ 6} = \frac{3}{64\pi^5} \times \frac{h^4 c^4}{K^2} \sigma_A \eta_S \int_0^\infty \frac{\varepsilon_S(E)\alpha_A(E)}{E^4} dE \qquad (22)$$

where h and c are the Planck constant and the velocity of light, respectively, and the K is the dielectric constant of the material. σ_A is the total A center absorption cross section and η_S is the emission efficiency of the S center. $\varepsilon_S(E)$ and $\alpha_A(E)$ are the emission spectrum of S center and absorption spectrum of A centre, respectively (Fig. 13).

3.2 The basic properties of Mn^{2+}

In the last few years, non-rare earth-based eco-friendly phosphors prepared under milder conditions have received increasing interest.[69] The outer electronic structure of Mn^{2+} is 3d^{5}4s^2.[70,71] On the basis of the Mn^{2+} Tanabe–Sugano diagram, the emission of Mn^{2+} can be easily changed from green to deep red by transforming the crystal field strength. Because the transition is $^4T_1 \rightarrow ^6A_1$, Mn^{2+} has broad band emission in the visible range, depending on the crystal field. Octahedral coordinated Mn^{2+} shows an orange to red emission, while tetrahedral
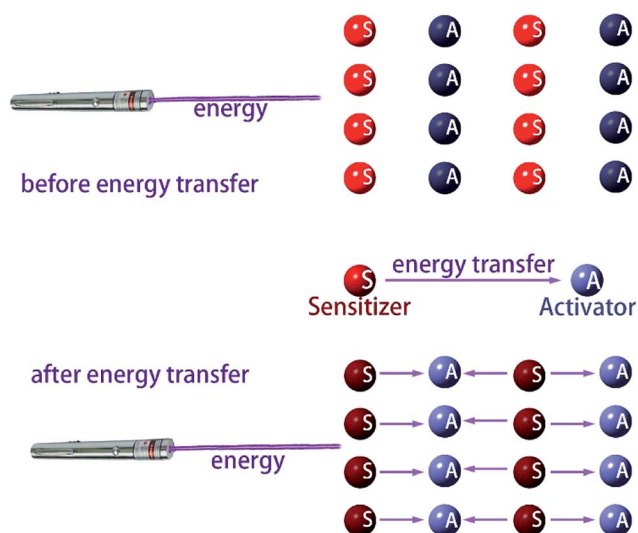
Fig. 13 Schematic diagram of the energy transfer, the dark and light colors indicate the level of energy.

coordinated Mn^{2+} shows green emission. The luminescence spectrum of Mn^{2+} consists of a structureless band at peak wavelengths of 490–750 nm, with the half width of 1000–2500 cm^{-1}. In general, the crystal field at a tetrahedral site is weaker than that of an octahedral site. When Mn^{2+} is in a weak crystal field, the splitting of the excited energy in orbitals is small, resulting in a higher energy of Mn^{2+} emission, but its energy is low. Generally, when Mn^{2+} is substituted for alkaline-earth metals (Ga^{2+}, Sr^{2+},

Ba^{2+}), the larger lattice distortion is not conducive to the direct excitation of Mn^{2+}, which makes it difficult to achieve direct luminescence. Therefore, Mn^{2+} is not suitable for individually serving as an activator with low luminescence efficiency.

Though Mn^{2+} ions emit red light from $d \rightarrow d$ transitions, the $4T_1(4G) \rightarrow 6A_1(6S)$ emission in the 3d electron configuration is weak because it is forbidden, which leads to weak absorption in the ultraviolet region and disparate fluorescence properties in different hosts. However, on introducing Eu^{2+} or Ce^{3+} as co-activators, the excitation of Mn^{2+} is covered by the emission of Eu^{2+} or Ce^{3+}, which creates the necessary conditions for vibrational transmission, i.e., there is overlap between the emission of the activator and the excitation of the sensitizer. Meanwhile, there may be energy transfer between the sensitizer and activator. On the basis of the resonance energy transfer mechanism, the excitation energy of the sensitizer can induce the activator to emit fluorescence, while the fluorescence intensity decays. White light can be obtained by co-doping Ce^{3+}/Mn^{2+} or Eu^{2+}/Mn^{2+} under effective resonance-type energy transfer; a schematic diagram of energy transfer is shown in Fig. 14.[72–74]

3.3 The co-doping of Ce^{3+}/Mn^{2+}

The outer electronic structure of Mn^{2+} is $3d^5$, which presents typical d–d transitions when excited. Its photoluminescence range changes from 500 to 700 nm, which depends on the crystal field environment; however the d–d transition of Mn^{2+} is forbidden by the selection rules, and the luminescence is very weak since it can only be indirectly excited using sensitized ions or the substrate itself for energy transfer. A large number of
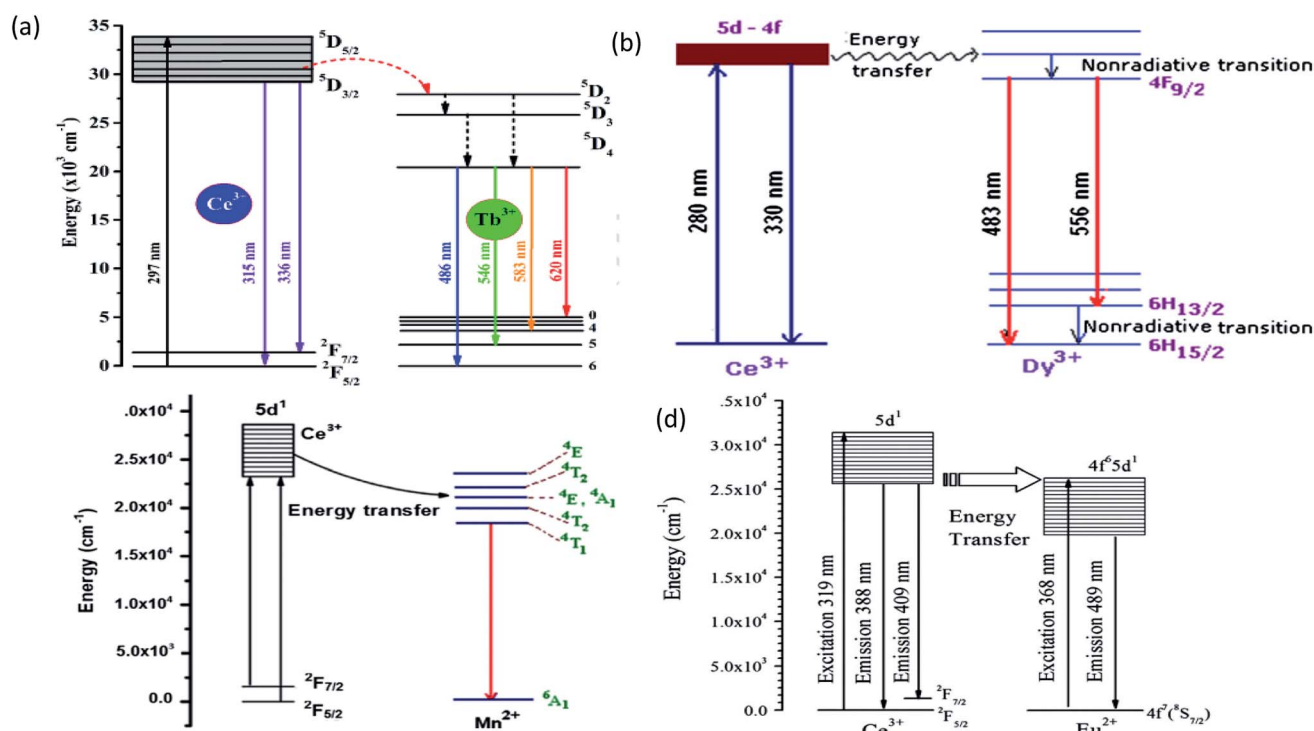
Fig. 14 (a) The schematic energy level diagram for the energy transfer process in the $BaMgF_4:Ce_x^{3+},Tb_y^{3+}$ phosphors.[75] (b) Energy level diagram of $KNaSO_4:Ce,Dy$.[79] (c) Energy transfer diagram of $Ce^{3+} \rightarrow Mn^{2+}$.[82] (d) Schematic energy-level diagram of Ce^{3+} and Eu^{2+}.[85]

studies have been conducted on the mechanism of energy transfer, e.g., $Ce^{3+} \rightarrow Tb^{3+}$, $Ce^{3+} \rightarrow Mn^{2+}$, $Ce^{3+} \rightarrow Dy^{3+}$ $Ce^{3+} \rightarrow Eu^{2+}$, etc., as shown in Table 4, which indicates that the Ce^{3+} ion is a highly efficient ion. The energy level diagram of the energy transfer about Ce is shown in Fig. 14.

The outermost electron configuration of Ce^{3+} is $4f^1$, which can change to a lower energy level of 5d when absorbing energy. The 5d electronic excited state is different from the 4f electronic state, which is easily shielded by $5s^2 5p^6$, resulting in the crystal field having a great influence on it, so the 4f–5d transition of Ce^{3+} in the 200–400 nm spectral region often exhibits strong absorption and excitation spectra.

$Ca_2Gd_8(SiO_4)_6O_2$:Ce^{3+},Mn^{2+} has been prepared by Li et al.,[86] and the emission spectra are shown in Fig. 15 for different concentrations of Ce^{3+} and Mn^{2+}. The phosphors emit blue to white light, and with the increased Mn^{2+} concentration, there was complete conversion to yellow light when excited by UV irradiation, due to the 5d–4f transition of Ce^{3+} and the $^4T_1 \rightarrow {}^6A_1$ transition of Mn^{2+}, respectively. It is noteworthy that the emission peaks of Mn^{2+} have a slightly red shift from 564 nm to 570 nm. The Ce^{3+} ion simultaneously occupies the 4f and 6h sites in the $Ca_2Gd_8(SiO_4)_6O_2$ host, and gives different blue emission under different UV excitation. Energy transfer from $Ce^{3+} \rightarrow Mn^{2+}$ also exists in the phosphor, hence, via precise control of the contents of Mn^{2+} and Ce^{3+}, a wide-range white emission can be obtained. On the other hand, changing excitation sources is another way to obtain the color-tunable emission in a signal phase host. PLE and PL spectra of the LEDs (light emitting diodes) and FEDs (field emission displays) of the Ce^{3+}, Mn^{2+} co-doped phosphors, $NaCaBO_3$:Ce^{3+},Mn^{2+} were also studied, which have potential applications in the field of white EDS. It has been shown that for the crystal structure of $NaCaBO_3$, the relative PL intensity of blue to yellow emission increases with the increase of the excitation wavelength from 287 to 330 nm. Moreover, $Ca_2Gd_8(SiO_4)_6O_2$:Ce^{3+},Mn^{2+}, has a good CL coefficient (K/S) relation, which was used to calculate the measured reflectance (R) for $NaCaBO_3$, to probe the absorption of the host lattice.[87]

$$F(R) = \frac{(1-R)^2}{2R} = \frac{K}{S} \qquad (23)$$
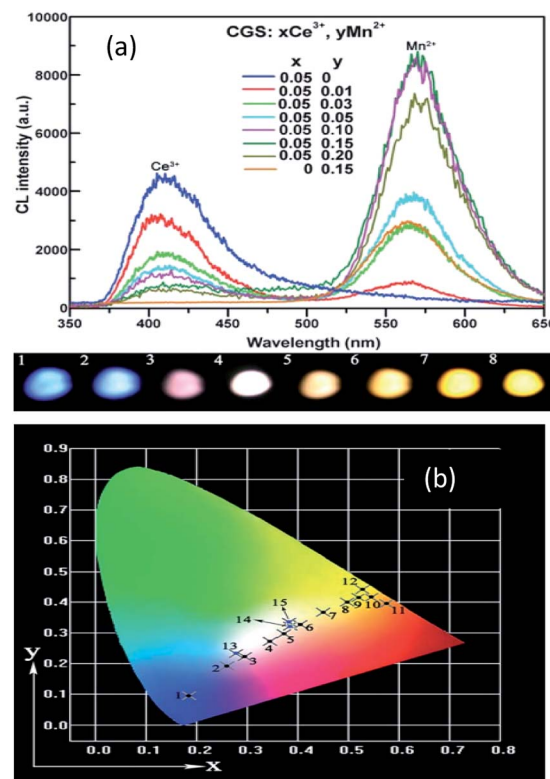
Fig. 15 (a) Emission spectra and luminescence properties of CGS:xCe^{3+},yMn^{2+} samples. (b) The CIE chromaticity diagram for $Ca_2Gd_8(SiO_4)_6O_2$:0.05Ce^{3+},yMn^{2+} samples under 287 nm UV excitation.[86]

where R, K, and S represent the reflectance, absorption coefficient, and scattering coefficient, respectively. Hence, the band gap of the $NaCaBO_3$ host was calculated to be approximately 4.48 eV by extrapolation, essentially owing to the transition between the valence band and the conduction band in this host.[88]

From Fig. 16(1) and (2), it is seen that there exists a spectral overlap between the PL spectrum of $NaCa_{0.99}BO_3$:0.01Ce^{3+} and the PLE spectrum of $NaCa_{0.96}BO_3$:0.03Mn^{2+}, indicating that a resonance-type energy transfer from the Ce^{3+} to Mn^{2+} ions is expected in the co-doped sample. Due to the energy transfer

Table 4 The energy transfer about Ce^{3+} in different hosts and doping ions

Host	Energy transfer	λ_{ex} (nm)	λ_{em} (nm)	Ref.
$BaMgF_4$	$Ce^{3+} \rightarrow Tb^{3+}$	297	488, 545, 584	75
$Ca_{10}(PO_4)_6S$	$Ce^{3+} \rightarrow Tb^{3+}$	280, 430, 545	410, 550	76
$Sr_2MgSi_2O_7$	$Ce^{3+} \rightarrow Tb^{3+}$	228	542	77
$Sr_3Gd_2(Si_3O_9)_2$	$Ce^{3+} \rightarrow Tb^{3+}$	348	540, 550	78
$KNaSO_4$	$Ce^{3+} \rightarrow Dy^{3+}$	280	330, 483, 556	79
$(Dy_{0.03}Ce_xY_{0.97-x})_3Al_5O_{12}$	$Ce^{3+} \rightarrow Dy^{3+}$	327, 367	496, 582	80
$Mg_3Ca_3(PO_4)_4$	$Ce^{3+} \rightarrow Mn^{2+}$	362, 410, 418	352, 645	81
$K_2AEP_2O_7$ (AE = Ca, Sr)	$Ce^{3+} \rightarrow Mn^{2+}$	320	534, 539	82
$Ca_4(PO_4)_2O$	$Ce^{3+} \rightarrow Eu^{2+}$	350	460, 630	83
$Ca_4Y_6O(SiO_4)_6$	$Ce^{3+} \rightarrow Eu^{2+}$	356, 280	426, 527	84
$Na_3Ca_6(PO_4)_5$	$Ce^{3+} \rightarrow Eu^{2+}$	319	391, 487	85

Fig. 17 (1) Excitation and emission spectra of CMPF:0.18Eu^{2+} (a), CMPF:0.18Mn^{2+} (b), and CMPF:0.18Eu^{2+},0.18Mn^{2+} (c) phosphors. The corresponding spectral overlap is also presented in the colored area. (2) Decay curves and lifetimes of Eu^{2+} in representative samples of CMPF:0.18Eu^{2+},yMn^{2+} (monitored at 454 nm and excited at 300 nm). (3) Variation of emission intensity for CMPF:0.18Eu^{2+},yMn^{2+} (y = 0–0.38) phosphors on Mn^{2+} doping content excited at 365 nm. (4) CIE chromaticity coordinates of CMPF:0.18Eu^{2+},yMn^{2+} samples (A–H corresponds to y = 0, 0.02, 0.06, 0.10, 0.18, 0.26, 0.34, respectively). The luminescence photographs of corresponding phosphors excited under a 365 nm UV lamp are shown on the right of the picture.[94]

reaching a maximum at x = 7 mol%, and then decreased when x exceeded 7 mol%, due to the concentration quenching effect. It was demonstrated that the mechanism of energy transfer is an electric dipole–quadrupole interaction from sensitizer Eu^{2+} to an activator Mn^{2+}. Fig. 16 provides a summary of the CIE chromaticity corresponding to the emission spectra excited by 380 nm, which indicates that changing the Mn^{2+} concentration can tune the color from blue through white light and eventually to red in the visible spectral region. The electroluminescence spectrum of white LED lamps fabricated using a NUV 405 nm chip combined with a single-phase white-emitting phosphor KCaY(PO$_4$)$_2$:1% Eu^{2+},4%Mn^{2+} driven by a 350 mA current is shown in Fig. 18. The correlated color temperature is 6507 K and CIE color coordinates are (0.314, 0.329), which indicate that the composition-optimized KCaY(PO$_4$)$_2$:1%Eu^{2+},4%Mn^{2+} phosphor may have promising applications for white-light NUV LEDs.[95]

4   Summary and outlook

Due to the characteristics of the transition metal electronic orbitals, Mn has many valence states, with Mn^{2+} and Mn^{4+}

being the most common. As activated ions, they have a wide range of applications. Mn^{4+} doped materials can work as a complement to the commercial phosphor powder "blue chips + Y$_3$Al$_5$O$_{12}$:Ce^{3+} (YAG:Ce)" to make up for the lack of red component, in order to improve the color rendering indexes and the correlated color temperature. They have the advantages of a simple preparation route and low-cost. Mn^{4+} activated oxide and fluoride red phosphors have attracted more and more attention, but low resistance to moisture and unclear structure-related luminescence mechanisms limit their rapid progress in scientific investigation and application of WLED lighting.

Ce^{3+}/Mn^{2+},Eu^{2+}/Mn^{2+} co-doped materials can produce color tunable phosphors in order to achieve UV excitable single mechanism phosphors to produce white light. In recent years, a single host material emitting white light has made significant progress. In order to further improve its performance, some more studies need to be conducted. Double-doped materials have some deficiencies in the spectral distribution; for example, Eu^{2+}/Mn^{2+} or Ce^{3+}/Mn^{2+} doped systems in the green emission region are relatively weak, which is certain

Fig. 18 (a) Photoluminescence excitation/photoluminescence (PLE/PL) spectra of the as-synthesized $KCaY(PO_4)_2$:1%Eu^{2+} phosphor. The inset shows the PL intensity of $KCaY(PO_4)_2$:Eu^{2+} phosphors as a function of Eu^{2+} concentration. (b) PLE spectrum of $KCaY(PO_4)_2$:1%Mn^{2+} and PL spectrum of $KCaY(PO_4)_2$:1%Eu^{2+}. (c) PL spectra of a series of $KCaY(PO_4)_2$:1%Eu^{2+},x%Mn^{2+} phosphors with different Mn^{2+} concentrations (x = 0, 1, 2, 4, 5, 7, and 10 mol%), excited at 365 nm. Inset shows the energy transfer efficiency from Eu^{2+} to Mn^{2+}, as a function of Mn^{2+} content. (d) Electroluminescence spectra of white LED lamps fabricated using a NUV 405 nm chip combined with a white-emitting $KCaY(PO_4)_2$:1%Eu^{2+},4% Mn^{2+} phosphor driven by a current of 350 mA. Inset shows a photo of the LED package.[95]

to affect the luminescence. Further research is being conducted on how to improve the spectral distribution of dual-doping systems, and how to meet the needs of different white phosphors.

In addition, due to the splitting of the Mn^{2+} energy level, the emission spectrum can be red shifted to produce deep red and near infrared light. It has been widely used in the fields of optical fiber communication, solid state lasers, light emitting markers and fluorescence immunoassays.

Acknowledgements

References

1 H. M. Zhang, H. R. Zhang, Y. L. Liu, J. K. Deng, B. F. Lei, L. h. Liu, H. Y. Luo and X. Bai, *J. Alloys Compd.*, 2016, **688**, 1225–1232.
2 K. C. Mondal and J. Manam, *J. Mol. Struct.*, 2016, **1125**, 503–513.
3 S. X. Li, L. Wang, Q. Q. Zhu, D. M. Tang, X. J. Liu, G. F. Cheng, L. Lu, T. Takeda, N. Hirosaki, Z. R. Huanga and R. J. Xie, *J. Mater. Chem. C*, 2016, **4**, 11219–11230.
4 B. Yuan, Y. H. Song, Y. Sheng, K. Y. Zheng, X. Q. Zhou, P. C. Ma, X. C. Xu and H. F. Zou, *J. Solid State Chem.*, 2016, **47**(2), 169–177.
5 D. C. Huang, Y. F. Zhou, W. T. Xu, K. Wang, Z. G. Liu and M. C. Hong, *J. Alloys Compd.*, 2015, **653**, 148–155.

6 D. Q. Chen, W. D. Xiang, X. J. Liang, J. S. Zhong, H. Yu, M. Y. Ding, H. W. Lu and Z. G. Ji, *J. Eur. Ceram. Soc.*, 2015, **35**, 859–869.

7 W. G. Xiao, X. Zhang, Z. D. Hao, G. H. Pan, Y. S. Luo, L. G. Zhang and J. H. Zhang, *Inorg. Chem.*, 2015, **54**(7), 3189–31195.

8 L. L. Wei, C. C. Lin, M. H. Fang, M. G. Brik, S. F. Hu, H. Jiao and R. S. Liu, *J. Mater. Chem. C*, 2015, **3**, 1655–1660.

9 L. Chen, R. H. Liu, W. D. Zhuang, Y. H. Liu, Y. S. Hu, X. F. Zhou and X. L. Ma, *J. Alloys Compd.*, 2015, **627**(13), 218–221.

10 G. Blasse and B. C. Grabmaier, *Luminescent Materials*, Springer, Verlag, Berlin, Heidelberg, 1994, p. 113.

11 S. H. Kwon, B. K. Moon, B. C. Choi, J. H. Jeong and J. H. Kim, *J. Korean Phys. Soc.*, 2016, **68**(2), 363–367.

12 Z. Y. Mao, J. J. Chen, J. Li and D. J. Wang, *Chem. Eng. J.*, 2016, **284**, 1003–1007.

13 J. Chen, Y. G. Liu, L. F. Mei, Z. Y. Wang, M. H. Fang and Z. H. Huang, *J. Mater. Chem. C*, 2015, **3**(21), 5516–5523.

14 D. C. Huang, Y. F. Zhou, W. T. Xu, K. Wang, Z. G. Liu and M. C. Hong, *J. Alloys Compd.*, 2015, **625**, 148–155.

15 K. X. Song, J. X. Zhang, Y. F. Liu, C. H. Zhang, J. Jiang, H. C. Jiang and H. B. Qin, *J. Phys. Chem. C*, 2015, **119**(43), 24558–24563.

16 W. Xu, G. Zhu, X. Zhou and Y. Wang, *Dalton Trans.*, 2015, **44**(19), 9241–9250.

17 H. N. Luitel, R. Chand, T. Watari, T. Torikai and M. Yada, *RSC Adv.*, 2015, **5**(22), 17034–17040.

18 M. Y. Peng, X. W. Yin, P. A. Tanner, C. Q. Liang, P. F. Li, Q. Y. Zhang and J. R. Qiu, *J. Am. Ceram. Soc.*, 2013, **96**(9), 2870–2876.

19 S. Sugano, Y. Tanabe and H. Kamimura, *Multiplets of Transition Metal Ions in Crystals*, New brk: Academic Press, 1970.

20 R. P. Cao, K. N. Sharafudeen and J. R. Qiu, *Spectrochim. Acta, Part A*, 2014, **117**, 402–405.

21 M. G. Brik and A. M. Srivastava, *J. Lumin.*, 2013, **133**, 69–72.

22 H. M. Zhu, C. C. Lin, W. Q. Luo, S. T. Shu, Z. G. Liu, Y. S. Liu, J. T. Kong, E. Ma, Y. G. Cao, R.-S. Liu and X. Y. Chen, *Nat. Commun.*, 2014, **5**, 1–10.

23 D. Q. Chen, Y. Zhou, W. Xu, J. S. Zhong, Z. G. Ji and W. D. Xiang, *J. Mater. Chem. C*, 2016, **4**, 1704–1712.

24 M. G. Brik, S. J. Camardello and A. M. Srivastava, *ECS J. Solid State Sci. Technol.*, 2015, **4**, R39–R43.

25 T. Takahashi and S. Adachi, *J. Electrochem. Soc.*, 2008, **155**, 183–188.

26 A. M. Srivastava, *Opt. Mater.*, 2009, **31**, 881–885.

27 M. G. Brik, A. M. Srivastava and N. M. Avram, *J. Lumin.*, 2011, **131**, 54–58.

28 M. Y. Peng, X. W. Yin, P. A. Tanner, M. G. Brik and P. F. Li, *J. Am. Chem. Soc.*, 2015, **27**, 2938–2945.

29 P. F. Li, L. Wondraczek, M. Y. Peng and Q. Y. Zhang, *J. Am. Ceram. Soc.*, 2016, **99**(10), 3376–3381.

30 W. Li, H. R. Zhang, S. Chen, Y. L Liu, J. L Zhuang and B. F. Lei, *Adv. Opt. Mater.*, 2016, **4**(3), 427–434.

31 X. Ding, G. Zhu, W. Y. Geng, Q. Wang and Y. H. Wang, *Inorg. Chem.*, 2016, **55**(1), 154–162.

32 K. Li, D. Zhu and R. V. Deun, *Dyes Pigm.*, 2017, **142**, 69–76.

33 Y. X. Pan and G. K. Liu, *J. Lumin.*, 2011, **131**(3), 465–468.

34 M. G. Brik, Y. X. Pan and G. K. Liu, *J. Alloys Compd.*, 2011, **509**(5), 1452–1456.

35 X. L. Gao, Y. Song, G. X. Liu, X. T. Dong, J. X. Wang and W. S. Yu, *Dalton Trans.*, 2016, **45**(44), 17886–17895.

36 T. C. Lang, T. Han, L. L. Peng and M. J. Tu, *Mater. Chem. Front.*, 2017, **1**, 928–932.

37 T. T. Deng, E. H. Song, J. Su, L. Y. Wang, Y. Deng, S. Ye, J. Wang and Q. Zhang, *J. Mater. Chem. C*, 2017, **5**, 2910–2918.

38 R. Cao, M. Peng, E. Song and J. Qiu, *ECS J. Solid State Sci. Technol.*, 2012, **1**(4), R123–R126.

39 Z. liu, M. Yuwen, J. Liu, C. Yu, T. Xuan and H. Li, *Ceram. Int.*, 2017, **43**(7), 5674–5679.

40 R. P. Cao, D. Ceng, X. G. Yu, S. L. Guo, Y. F. Wen and G. T. Zheng, *Funct. Mater. Lett.*, 2015, **8**(5), 1550046.

41 P. F. Li, L. Wondraczek, M. Y. Peng and Q. Y. Zhang, *J. Am. Ceram. Soc.*, 2016, **99**(10), 3376–3381.

42 E. Song, J. Wang, J. Shi, T. Deng, S. Ye, M. Peng, J. Wang, L. Wondraczek and Q. Zhang, *ACS Appl. Mater. Interfaces*, 2017, **9**(10), 8805–8812.

43 A. Abdukayum, J. T. Chen, Q. Zhao and X. P. Yan, *J. Am. Chem. Soc.*, 2013, **135**(38), 14125–14133.

44 Q. H. Zhang, J. Wang, G. G. Zhang and Q. Su, *J. Mater. Chem.*, 2009, **19**, 7088–7092.

45 Y. X. Zhuang, Y. Katayama, J. Ueda and S. Tanabe, *Opt. Mater.*, 2014, **36**, 1907–1912.

46 J. Yan, M. G. Brik, C. M. Liu, D. J. Hou, W. J. Zhou, B. B. Zhang, Y. Huang, Y. Tao and H. B. Liang, *Opt. Mater.*, 2015, **43**, 59–65.

47 C. J. Duan, A. C. A. Delsing and H. T. Hintzen, *Chem. Mater.*, 2009, **21**, 1010–1016.

48 S. K. Singh, *RSC Adv.*, 2014, **4**(102), 58674–58698.

49 X. R. Zhong, X. P. Meng, M. Y. Li, X. Q. Wang, X. J. Wen and X. Y. Zhang, *Chem. Phys. Lett.*, 2012, **536**, 55–60.

50 C. M. Abreu, R. S. Silva, M. E. G. Valerio and Z. S. Macedo, *J. Solid State Chem.*, 2013, **200**, 54–59.

51 Y. Katayama, J. Ueda and S. Tanabe, *Opt. Mater. Express*, 2014, **4**, 613–623.

52 J. G. Cheng, P. L. Li, Y. S. Sun, Q. Y. Bai, Z. L. Li, M. M. Tian, C. Wang and Z. P. Yang, *J. Mater. Chem. C*, 2017, **5**, 127–133.

53 A. Bessiére, A. Lecointre, R. A. Benhamou, E. Suard, G. Wallez and B. Viana, *J. Mater. Chem. C*, 2013, **1**(6), 1252–1259.

54 A. Bessière, R. A. Benhamou, G. Wallez, A. Lecointre and B. Viana, *Acta Mater.*, 2012, **60**, 6641–6649.

55 Y. Y. Ma, J. Q. Hu, E. H. Song, S. Ye and Q. Zhang, *J. Mater. Chem. C*, 2015, **3**, 12443–12449.

56 L. Wu, B. Wang, Y. Zhang, L. Li, H. R. Wang, H. Yi, Y. F. Kong and J. J. Xu, *Dalton Trans.*, 2014, **43**, 13845–13851.

57 B. S. Choia, O. G. Jeonga, J. C. Parka, J. W. Kimb, S. J. Leeb, J. H. Ryuc, J. Leec and H. Chob, *J. Ceram. Process. Res.*, 2016, **17**(7), 778–781.

58 L. Hu, Q. Wang, X. Wang, Y. Li, Y. Wang and X. Peng, *RSC Adv.*, 2015, **5**, 104708–104714.

59 X. Ding, G. Zhu, Q. Wang and Y. Wang, *RSC Adv.*, 2015, **5**, 30001–33004.

60 Y. Pan, L. Li, J. Lu, R. Pang, L. Wan and S. Huang, *Dalton Trans.*, 2016, **45**, 9506–9512.

61 X. Zhu, Y. Yao and Z. Zhou, *Opt. Mater.*, 2016, **62**, 104–109.

62 R. Cao, D. Peng, H. Xu, S. Jiang, Z. Luo, H. Ao and P. Liu, *J. Lumin.*, 2016, **178**, 388–391.

63 K. W. Park, H. S. Lim, S. W. Park, G. Deressa and J. S. Kim, *Chem. Phys. Lett.*, 2015, **636**, 141–145.

64 B. Chandra Babu, B. Vengla Rao, M. Ravi and S. Babu, *J. Mol. Struct.*, 2017, **1127**, 6–14.

65 K. Omri and L. El Mir, *J. Mater. Sci.: Mater. Electron.*, 2016, **27**(9), 9476–9482.

66 E. H. Song, S. Ding, M. Wu, S. Ye, F. Xiao, S. F. Zhou and Q. Y. Zhang, *Adv. Opt. Mater.*, 2014, **2**, 670–678.

67 C. R. Ronda and T. Amrein, *J. Lumin.*, 1996, **69**, 245–248.

68 M. S. Kwon, J. H. Jordahl, A. W. Phillips, K. Chung, S. Lee, J. Gierschner, J. Lahann and J. Kim, *Chem. Sci.*, 2016, **7**(3), 2359–2363.

69 M. Y. Peng, X. W. Yin, P. A. Tanner, C. Q. Liang, P. F. Li, Q. Y. Zhang and J. R. Qiu, *J. Am. Ceram. Soc.*, 2013, **96**(9), 2870–2876.

70 J. Lü, F. Du, R. Zhu, Y. Huang and H. J. Seo, *J. Mater. Chem.*, 2011, **21**, 16398–16405.

71 M. Szumera, I. Wacławska and J. Sułowska, *J. Therm. Anal. Calorim.*, 2016, **123**(2), 1083–1089.

72 C. Wang, P. L. Li, Z. J. Wang, Y. S. Sun, J. G. Cheng, Z. L. Li, M. M. Tian and Z. P. Yang, *Phys. Chem. Chem. Phys.*, 2016, **18**, 28661–28673.

73 Z. Zhang and W. Tang, *J. Alloys Compd.*, 2015, **663**, 731–737.

74 J. Zhou, T. Wang, X. Yu, D. Zhou and J. Qiu, *Mater. Res. Bull.*, 2016, **73**, 1–5.

75 B. P. Kore, S. Tamboli, N. S. Dhoble, A. K. Sinha, M. N. Singh, S. J. Dhoble and H. C. Swart, *Mater. Chem. Phys.*, 2016, **187**, 233–244.

76 C. Liang, H. P. You, Y. B. Fu, X. M. Teng, K. Liu and J. H. He, *Optik*, 2017, **131**, 335–342.

77 Y. Hong, J. L. Chen, Y. Pu, T. J. Zhang and S. C. Gan, *J. Rare Earths*, 2015, **33**(4), 366–370.

78 Y. Zhu, Y. Liang, S. Liu, K. Li, X. Wu and R. Xu, *J. Rare Earths*, 2017, **35**(1), 41–46.

79 U. Manik, S. C. Gedamb and S. J. Dhoble, *Luminescence*, 2014, **30**(6), 910–913.

80 R. L. Zheng, D. W. Luo, Y. Yuan, Z. Y. Wang, Y. Zhang, W. Wei, L. B. Kong and D. Y. Tang, *J. Am. Ceram. Soc.*, 2015, **98**(10), 3231–3235.

81 J. Zhang, F. Zhang and L. L. Han, *J. Rare Earths*, 2015, **33**(8), 820–824.

82 L. R. Hatwar, S. P. Wankhede, S. V. Moharil, P. L. Muthald and S. M. Dhopte, *Luminescence*, 2015, **30**(6), 904–909.

83 Y. Q. Li, H. P. Ma, Y. J. Hua, Q. H. Yang, C. X. Li, D. G. Deng and S. Q. Xu, *J. Rare Earths*, 2016, **34**(1), 7–11.

84 P. L. Li, Z. J. Wang, Q. L. Guo and Z. P. Yang, *J. Am. Ceram. Soc.*, 2014, **98**(2), 495–500.

85 F. Zhang and W. J. Tang, *Luminescence*, 2014, **30**(2), 216–220.

86 G. G. Li, D. L. Geng, M. M. Shang, C. Peng, Z. Y. Cheng and J. Lin, *J. Mater. Chem.*, 2011, **21**, 13334–13344.

87 Y. Kim, K. Page, A. Limarga, D. Clarke and R. Seshadri, *Phys. Rev. B: Condens. Matter Mater. Phys.*, 2007, **76**, 115204.

88 J. F. Sun, W. L. Zhang, Y. M. Shi, D. Z. Shen and J. Y. Sun, *J. Electrochem. Soc.*, 2012, **159**, J5–J12.

89 J. F. Sun, Z. P. Lian, G. Q. Shen and D. Z. Shen, *RSC Adv.*, 2013, **3**, 18395–18405.

90 Z. Chen, J. Zhang, S. Chen, M. Lin, C. He, G. Xu, M. Wang, X. Yu, J. Zou and K. Guo, *J. Alloys Compd.*, 2015, **632**, 756–759.

91 Z. J. Wang, S. Q. Lou, P. L. Li and Z. G. Lian, *Opt. Mater. Express*, 2017, **56**(4), 1167–1172.

92 J. Barzowska, Z. G. Xia, D. Jankowski, D. Włodarczyk, K. Szczodrowski, C. G. Ma, M. G. Brik, Y. Zhydachevskii and A. Suchocki, *RSC Adv.*, 2017, **7**, 275–284.

93 Y. M. Wang, H. B. Zhang, Q. L. Wei, C. H. Sua and D. Zhang, *Ceram. Int.*, 2016, **42**(10), 12422–12426.

94 K. Li, D. L. Geng, M. M. Shang, Y. Zhang, H. Z. Lian and J. Lin, *J. Phys. Chem. C*, 2014, **118**, 11026–11034.

95 W. R. Liu, C. H. Huang, C. W. Yeh, J. C. Tsai, Y. C. Chiu, Y. T. Yeh and R. S. Liu, *Inorg. Chem.*, 2012, **51**, 9636–9641.